Research Article

Numerical Simulation & Push-off Test Validation of Full-Depth Precast Bridge Decks with Large Stud Clusters in UHPC Shear Pockets

Kerati Suwanpakpraek
Department of Mechanical and Aerospace Engineering, Faculty of Engineering, King Mongkut's University of Technology North Bangkok, Bangkok, Thailand

Krissachai Sriboonma* and Sacharuck Pornpeerakeat
Department of Teacher Training in Civil Engineering, Faculty of Technical Education, King Mongkut's University of Technology North Bangkok, Bangkok, Thailand

Natawut Chaiwino
Department of Technical Education, Faculty of Technical Education, Rajamangala University of Technology Thanyaburi, Thailand

* Corresponding author. E-mail: krissachai.s@fte.kmutnb.ac.th
DOI: 10.14416/j.asep.2026.01.003
Received: 18 September 2025; Revised: 29 October 2025; Accepted: 12 December 2025; Published online: 12 January 2026
© 2026 King Mongkut's University of Technology North Bangkok. All Rights Reserved.

Abstract

Full-Depth Precast Concrete (FDPC) bridge deck panels are increasingly used in highway construction due to their rapid installation, ease of replacement, and cost-effectiveness. To improve composite action, clusters of large headed-stud connectors embedded in Ultra-High-Performance Concrete (UHPC) shear pockets have been introduced, however, this configuration often induces high stress concentrations and premature cracking around the pockets. This study develops and validates a finite element (FE) model of FDPC panels incorporating L-angle confined UHPC pockets with clustered large studs, based on push-off tests under eccentric loading. The FE simulations accurately reproduced experimental behavior, with predicted ultimate loads and crack patterns closely matching test results for specimens with a cluster of 4, 6, and 8 studs. Parametric analyses showed that finer mesh sizes (10–30 mm) improved crack localization but underestimated ultimate loads (up to 8.3%). Push-off stiffness was influenced by LVDT placement (with 10–20%) due to localized slip and by eccentric loading positions, which significantly affected shear capacity and premature crack pattern. L-angle confinement enhanced shear resistance by up to 15%. Comparisons with experimental data and American Association of State Highway and Transportation Officials (AASHTO) Load and Resistance Factor Design (LRFD) bridge design equations confirmed that the FE model provides a reliable and efficient analytical tool for optimizing FDPC bridge deck connections with large stud clusters and UHPC shear pockets.

Keywords: Finite element, Full-depth bridge deck panels, Large-sized headed stud, Numerical simulation, Push-off test, Ultra-High-Performance Concrete shear pockets

1 Introduction

The growing demand for durable, efficient, and rapidly constructible bridge systems has led to significant advancements in bridge deck technologies. Among these, the Full–Depth Precast Concrete (FDPC) bridge deck panel system has gained widespread adoption due to its ability to accelerate construction, minimize traffic disruption, and enhance structural durability [1]–[3]. Unlike conventional cast–in–place decks, FDPC decks are prefabricated offsite under controlled conditions, ensuring high–quality construction, reduced material waste, and improved long–term performance consistency [4], [5].

These panels are then assembled onsite and connected to supporting steel girders through shear connectors, which could be clustered as a group of studs and embedded within shear pockets filled with Normal Strength Concrete (NSC) or high strength cement or even better with Ultra–High–Performance Concrete (UHPC) [6]. Recent studies have also explored UHPC-filled shear pockets in Precast Concrete (PC) composite girders, highlighting their potential to further enhance system performance [7], [8].

UHPC is an advanced cementitious composite characterized by compressive strengths exceeding 120–150 MPa, exceptional durability, and superior tensile properties due to its dense microstructure and steel fiber reinforcement [9]. Compared to conventional concrete, UHPC offers higher resistance to cracking, freeze–thaw cycles, and chloride penetration, making it an ideal material for critical bridge connections [10]. When used as an infill material for shear pockets, UHPC facilitates efficient shear transfer between precast deck panels and steel girders, and thereby improving overall bridge deck integrity. However, the performance of UHPC–filled shear pockets in achieving effective composite behavior—particularly in terms of deck–to–pocket, pocket–to–stud, and deck–to–girder interactions—remains a subject of ongoing research [11]. Previous investigations comparing UHPC and NSC pockets in PC composite girders have revealed that cracking frequently occurs in NSC regions, and additional interface reinforcement may be required to optimize shear performance [7], [8].

To further enhance shear transfer efficiency between the concrete deck and steel girders, the present study focuses on UHPC shear pockets incorporating clusters of large-diameter headed studs (31.75 mm or 1.25"), rather than conventional smaller studs (≤ 19 mm or ¾"). The use of larger studs offers several advantages, including increased shear capacity, reduced connector density, and improved fatigue resistance [12]–[14]. Moreover, clustering large studs within UHPC pockets can decrease welding time and congestion while simplifying installation. Nonetheless, large-diameter studs may induce localized stress concentrations, stiffness variations, and potential cracking around the connection region [15].

To address these challenges, steel angle ring confinement has been proposed as an innovative reinforcement strategy for UHPC shear pockets. Traditional confinement methods, such as rebar reinforcement or steel mesh, may not fully capitalize on the superior strength of UHPC, while tubular confinement can be overdesigned for this system. In contrast, L–angle ring confinement provides enhanced lateral restraint, better stress distribution, and improved resistance to localized failure [16], [17]. When combined with UHPC pockets containing large–headed stud clusters, this confinement mechanism can mitigate premature cracking, improve ductility, and promote uniform load transfer, thereby extending the long–term performance of the bridge deck system. This approach is supported by experimental findings demonstrating improved behavior of L–angle confined shear pockets under both static [16], [17] and cyclic loading conditions [18].

Sriboonma *et al.*, [19] investigated the shear behavior of UHPC shear pockets with L–angle ring confinement and large–diameter stud clusters in FDPC systems through a series of push–off tests under eccentric loading. The study examined the effects of pocket dimensions (width and length) and stud arrangements (4, 6, and 8 large studs) on static shear performance. The findings demonstrated that failure modes and crack patterns occurred in NSC slab regions bearing against UHPC pocket. Shear strengths of samples were compared to the design equations according to AASHTO LRFD and Eurocode 4–where the compatible results matched with the specimens with 4–studs in a square shape pocket, while the others found less compatible from 3.6% to 9.4%. However, with the limited number of samples, in–depth analysis and comparison against the results of the samples with NSC shear pocket and/or without L–angle confinement were not performed.

Therefore, this study employs Finite Element Analysis (FEA) to extend previous research by investigating the structural efficiency of UHPC shear pockets with and without L–angle ring confinement. The analysis examines the effects of Linear Variable Differential Transformer (LVDT) positioning, eccentric loading, and compares UHPC and NSC pockets under push–off conditions. The developed FEA model is validated against experimental data in terms of shear strength, load–slip response, stress distribution, and failure mechanisms [20]. Additionally, parametric analyses are conducted to refine modeling parameters such as mesh size, material constitutive laws, Concrete Damage Plasticity (CDP) properties, and boundary conditions [21].

Ultimately, the findings of this study aim to contribute to further FEA development for UHPC shear pockets under fatigue or cyclic loading conditions. The outcomes will also support the design standards and implementation of Accelerated Bridge Construction (ABC) systems with enhanced efficiency, durability, and resilience.

2 Materials and Methods

2.1 *Specimen geometry of push-off experiment*

The specimens of FDPC bridge deck panels were cast in L–shape and tested under static push–off load. The specimen consisted of three main parts: FDPC panel, UHPC pocket and the clustered studs. The FDPC deck panel is 600 mm (24 in) wide, 1,100 mm (44 in) long, and 200 mm (8 in) thick, with the enlarged loading thickness about 500 mm (20 in) as shown in Figure 1. The second part is a cluster of large–sized studs with diameters of 31.75 mm (1¼ in) and 63.5 mm (2½ in) for the shank and the head sections, respectively, at 76.2 mm (3 in) spacing on center as shown in Figure 2(a), which was embedded inside the UHPC shear pocket. The dimensions of the shear pocket were based on the stud arrangement of 4, 6, and 8 studs, which varied from a rectangular shape of 12×9 inches, a square shape of 12×12 inches, and a rectangular shape of 12×15 inches, respectively, as shown in Figure 2(b). The shear pockets were cut through the thickness of the FDPC panel and were filled with UHPC materials. The additional parts included L–angle ring confinement, which was welded together with 25×25×3 mm steel angle and two 12 mm diameter deformed hook bars on each side around the perimeter to create extra concrete bonding. The last part is a 20 mm thick steel plate placed at the bottom of the specimen acting as a top flange of steel girders of a bridge. Also, the minimum reinforcement of the 12 mm diameter deformed bars was embedded inside the FDPC panel for all specimens.

Figure 1 presents the geometry of the L–shape FDPC deck panel and the variable configurations of three different types of shear pockets expressed in Table 1. The dimension of the FDPC panel was represented in transverse and longitudinal sections in Sections A–A and B–B of the figure, respectively. Three variable sizes (width P_W x length P_L) of shear pockets were considered, depending on the number of studs of 4, 6, and 8 studs in each cluster, which led to the specimens named P-4-9×12-U, P-6-12-U, and P-8-12×15-U for this study.

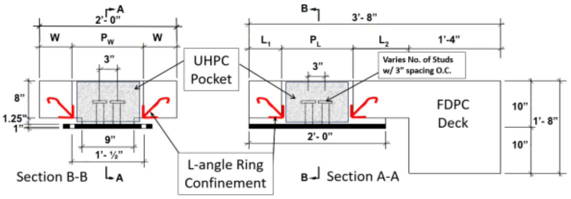

Figure 1: Geometry of experimental specimens.

Table 1: Dimension and configuration of experimental specimens.

Specimen	No. of Studs	$P_W \times P_L$ (inch × inch)	W (inch)	L_1 (inch)	L_2 (inch)
P-4-12×9-U	4	9×12	7.5	6	10
P-6-12-U	6	12×12	6	6	10
P-8-12×15-U	8	12×15	6	4.5	8.5

Though the sizes of the shear pockets were varied, the spacing of large-sized studs was the same for all specimens, as shown in Figure 2. The spacing of each stud was controlled by the minimum center–to–center spacing of 4.0 typical stud diameter of 19 mm (¾ in), which was 76.2 mm (3 in) in both transverse and longitudinal axes per AASHTO LRFD Bridge Design Specifications: section 6.10.10.1.3 [22]. The clear distance between the edge of the top flange and the edge of the nearest studs was greater than 25.4 mm (1.0 in), which was also followed by the design code. Noted, all studs were fillet-welded to the steel plate in three layers to ensure no failure due to welding tear-off.

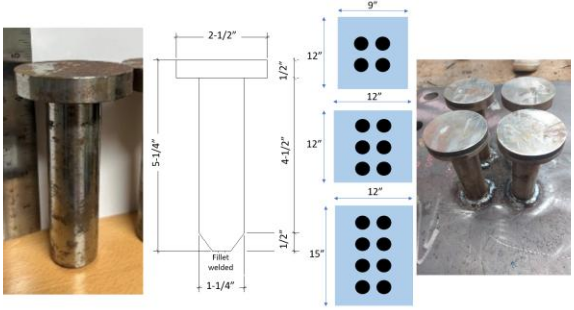

(a) (b)

Figure 2: Dimensions of large–sized headed studs, arrangement of clustered studs, and stud welding.

2.2 *Push–off test setup*

The specimen was initially fabricated by casting the FDPC deck, while the cluster of large–sized studs was welded to the steel plate. Then UHPC was poured into the shear pocket where the studs were embedded inside. The specimens were air-cured for 28 days before push–off testing. Bolted connection was proceeded between the base steel plate of the specimen and the balancing frame in the vertical direction. The hydraulic jack and load cell were then installed on the main steel frame and the enlarged area of the specimen (Figure 3) prior to loading. To monitor the displacement in both vertical (slip) and horizontal (tilt–up) direction, three LVDTs were attached to the specimen and the balancing frame. Moreover, two strain gauges were mounted to the angle ring confinement in the transverse and longitudinal axes to collect hoop strains around the confinement.

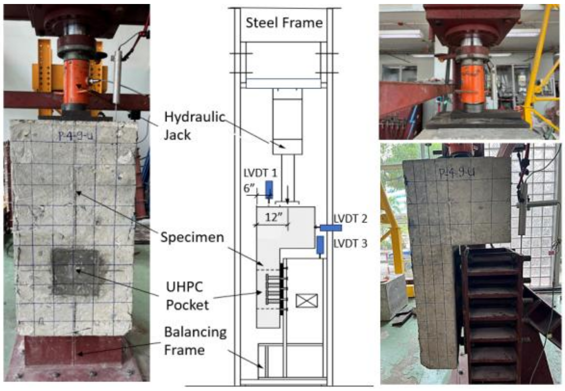

Figure 3: Push–off test set–up: front, side, and schematic view; and load cells and LVDTs setup.

2.3 *Material properties*

The FDPC deck panel was cast with 358 ksc (35 MPa) compressive cylinder strength of ready mixed concrete with minimum reinforcements of DB12 deformed bar grade SD40 (TIS) or equivalent to Grade 60 (AISC) embedded. The shear pocket was filled with 1,234 ksc (121 MPa) compressive cubical strength of UHPC with reactive powder and steel fiber 13 mm length and 0.20 mm diameter, as shown in the mixing proportion of UHPC in Table 2.

Table 2: UHPC mixed design proportion.

Description	Weight per Volume (kg/m^3)					
	Cement[1]	Silica fume	Sand	Water	Super plasticizer[2]	Steel fiber[3]
UHPC mixed design	900	225	1175	207	15	150
Cement Ratio	1.00	0.25	1.31	0.23	0.02	0.17
% per Weight	34.12	8.53	44.55	7.85[4]	0.57	5.69

Note 1: Low carbon Portland cement Type I
Note 2: Sika ViscονCrete-819 Extra
Note 3: Dramix OL 13/0.2
Note 4: 20% extra water added for low carbon cement

Steel angle grade SS540 (TIS) or equivalent A36 (AISC) was welded around the perimeter of the shear pocket to form the L–angle ring confinement. Also, two DB12 hook bars grade SD40 were welded to each side of the angle in a total of 8 hook bars around the confinement. The large–sized headed studs with SCM440 steel grade based on JIS G4105, which are commonly used for Thai Industrial Standards or equivalent to steel grade 1018 per Society of Automotive Engineers (SAE) standard, yield strength 65/85 ksi and tensile strength of 105/130 ksi, were used in this study. Table 3 summarizes the material properties used for each part of the specimen.

Table 3: Summary of material properties for push–off.

Description	Type/ Grade	Yield Strength	Ultimate Strength
Shear pocket	UHPC	1,234 ksc (17.55 ksi / 121.1 MPa)	1,234 ksc (17.55 ksi / 121.1 MPa)
Concrete slab	Normal Weight	358 ksc (5.09 ksi / 35.1 MPa)	358 ksc (5.09 ksi / 35.1 MPa)
Reinforcement / Hook bars	Deform SD40	2400 ksc (65 ksi/ 235.36 MPa)	4000 ksc (55 ksi / 392.27 MPa)
Studs	SCM440	4600 ksc (85 ksi/ 448.16 MPa)	7400 ksc (105 ksi / 723.95 MPa)
Angle confinement	SS540	2400 ksc (34 ksi / 235.36 MPa)	4000 ksc (55 ksi / 392.27 MPa)

2.4 *Basic information of the finite element model*

The finite element (FE) model was performed using ABAQUS/CAE standard module 2023 version. The model geometry was created according to the test specimen in Section 2.1. The components of the push–off test model included five (5) parts and five (5) materials model as shown in Table 3, which can be classified material models as follows:

1) Shear pocket: Concrete damage plasticity model
2) Concrete slab: Concrete damage plasticity model
3) Reinforcement/ Hook bars: Elastic-plastic model
4) Studs: Elastic-plastic model
5) Angle confinement: Elastic-plastic model

The details of constitutional laws and the simulation material model were presented in Section

2.7. Loads and boundary conditions were applied under similar test conditions in Section 2.5. The boundary and interaction condition of the push–off test model were presented in Section 0. The simulation model was simplified to a half model in a symmetrical X–Y plane. The element size and type were optimized for corrective results as per Section 2.6, which can reduce the number of meshes and implementation time. The push–off test model was presented in Figure 4.

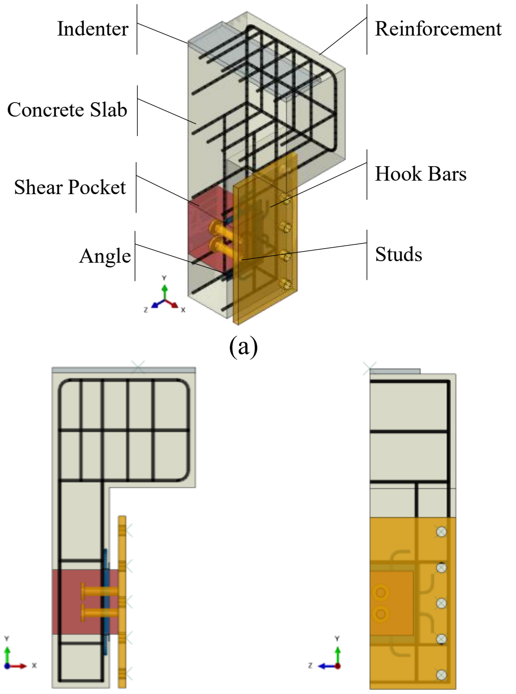

(a)

(b) (c)

Figure 4: Push–off test model: (a) components of push–off test model, (b) side view, (c) front view.

2.5 *Load and LVDT measurement location*

The location of load application and the LVDT measurement reflected the studded behavior of the push–off test. The load location had a direct influence on the ultimate load, which was investigated under four (4) loading conditions: starting at the half–depth (center) of the FDPC panel as 4" and followed by adding eccentricity of 6", 8", and 9" from the center. The LVDT measurement location influenced the deformation results of the test, which were considered under three points at distances of 4", 6", and 8" away from the front edge. The location of the load application and the LVDT measurement is presented in Figure 5. The effect of the eccentric load induced an additional moment, causing variable internal stresses, which were analyzed through the reactions of the model, namely the shear force (F_V) and the axial force (F_A).

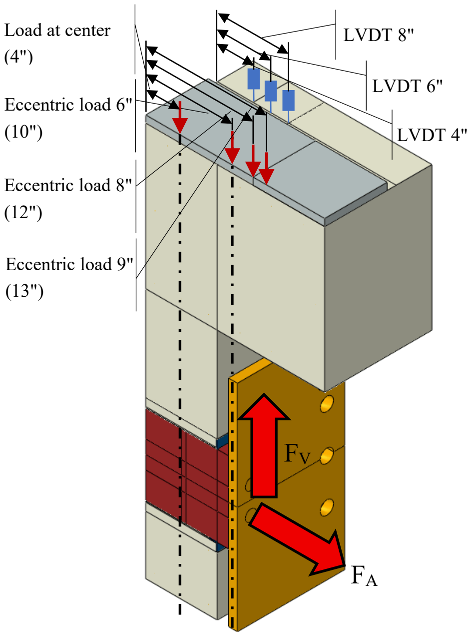

Figure 5: Model location of load and LVDT.

2.6 *Elements size and type*

The element types were divided into components of the shear pocket model, which included the shear pocket, concrete slab, studs, and angle confinement, as element types of C3D8. Reinforcement and hook bars were element types of B31. The C3D8 element is an 8-node linear brick element and the B31 element is a first-order, three-dimensional beam element [23]. The shear pocket, studs and angle confinement were meshed with element sizes less than 10 mm. The reinforcement and hook bars were meshed with an element size approximately equal to their diameter (12 mm). The mesh of the shear pocket and concrete slab was refined in the regions around the studs and at the UHPC–concrete slab interface to ensure accurate simulation with mesh sizes ranging from 10 to 30 mm as shown in
Figure **6**. This refinement was performed to assess the comparative effects of variable mesh sizes.

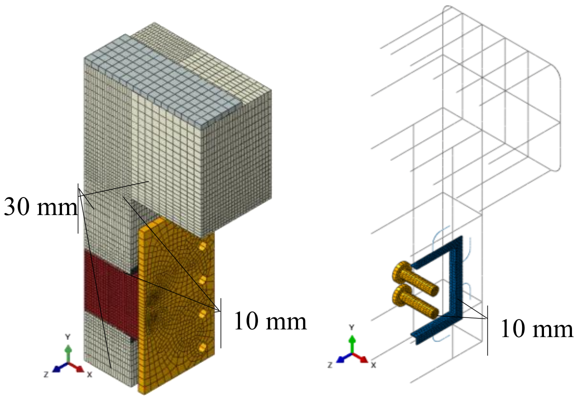

(a) (b)

Figure 6: Mesh model: (a) outside part, (b) inside part.

2.7 *Constitutional laws of materials*

2.7.1 *MPC stress-strain curve model*

The MPC stress-strain curve model was used to estimate the true stress-true strain curve of metal material [24]. This model can estimate strain hardening characteristics, which require input parameters of engineering yield stress and engineering ultimate stress in Table 3. The true stress–true strain curves of all materials were estimated using Equations (1) to (11) as shown in Figure 7.

$$\varepsilon_t = \frac{\sigma_t}{E_y} + \gamma_1 + \gamma_2 \tag{1}$$

Where,

$$\gamma_1 = \frac{\varepsilon_1}{2}(1.0 - tanh[H]) \tag{2}$$

$$\gamma_2 = \frac{\varepsilon_2}{2}(1.0 - tanh[H]) \tag{3}$$

$$\varepsilon_1 = \left(\frac{\sigma_t}{A_1}\right)^{\frac{1}{m_1}} \tag{4}$$

$$A_1 = \frac{\sigma_{ys}(1+\varepsilon_{ys})}{(ln[1+\varepsilon_{ys}])^{m_1}} \tag{5}$$

$$m_1 = \frac{ln[R] + (\varepsilon_p - \varepsilon_{ys})}{ln\left[\frac{ln[1+\varepsilon_p]}{ln[1+\varepsilon_{ys}]}\right]} \tag{6}$$

$$\varepsilon_2 = \left(\frac{\sigma_t}{A_2}\right)^{\frac{1}{m_2}} \tag{7}$$

$$A_2 = \frac{\sigma_{uts}\cdot exp[m_2]}{{m_2}^{m_2}} \tag{8}$$

$$H = \frac{2\left[\sigma_t - \left(\sigma_{ys} + K\cdot\left(\sigma_{uts} - \sigma_{ys}\right)\right)\right]}{K\left(\sigma_{uts} - \sigma_{ys}\right)} \tag{9}$$

$$K = 1.5R^{1.5} - 0.5R^{2.5} - R^{3.5} \tag{10}$$

$$R = \frac{\sigma_{ys}}{\sigma_{uts}} \tag{11}$$

σ_{ys} is the engineering yield stress, ε_{ys} is the engineering offset strain 0.2% [24], σ_{uts} is the engineering ultimate stress, σ_t is the true stress, ε_t is the true strain, m_2 is the curve fitting exponential parameter of ferritic steel using 0.60(1.00-*R*) [24], ε_p is the engineering offset strain for the proportional limit of ferritic steel of 2×10^{-5} [24].

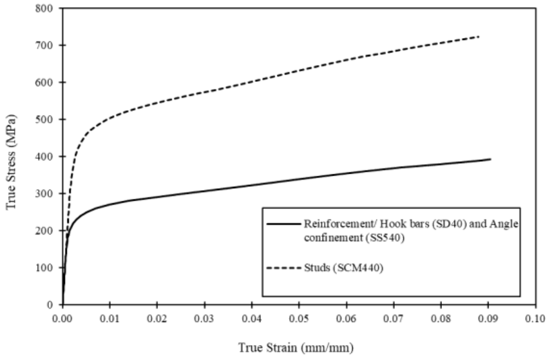

Figure 7: True stress-true strain curve.

2.7.2 *Full–depth concrete slab*

Among the most widely used constitutive models for regular concrete in compression and tension [25–29], the stress–strain diagram proposed by Carreira and Chu [26] was used to represent the uniaxial compressive behavior of concrete. The stress–strain relationship is expressed in Equations (12) to (13).

$$\frac{\sigma_c}{f_c'} = \frac{\beta(\varepsilon/\varepsilon_c')}{\beta - 1 + (\varepsilon/\varepsilon_c')^{\beta}} \tag{12}$$

$$\beta = \frac{1}{1 - \frac{f_c'}{\varepsilon_c' E_0}} \quad \text{for } \beta \geqslant 1 \text{ and } \varepsilon \leqslant \varepsilon_u \tag{13}$$

where a material parameter β depends on the shape of the stress-strain curve. Strain at the peak stress ε_0 is commonly taken as 0.002. ε_u is the ultimate strain of which a typical value is 0.003 for normal concrete.

The initial elastic modulus of concrete can be calculated as $E_0 = 4730\sqrt{f_c'}$ [30].

Tensile behavior of concrete was characterized by the model developed by Nayal and Rasheed [29] as shown in Figure 8(a). The ascending branch of the stress-strain curve is determined through the initial elastic modulus of concrete. Crack initiation and growth cause the sudden drop in the curve at the tensile strain ε_{cr} corresponding to the peak tensile stress, followed by two descending branches indicating primary and secondary cracking stages. Wahalathantri *et al.*, [31] modified the strain-softening portions of the stress-strain curve to prevent FEA run–time errors as illustrated in Figure 8(b). The responses of NSC in compression and tension according to the models mentioned above are depicted in Figure 9(a) and (b), respectively.

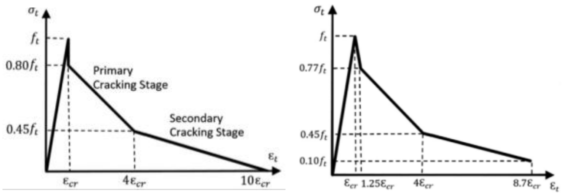

(a) (b)

Figure 8: Tensile stress–strain curves proposed by (a) Nayal and Rasheed [29] and (b) Wahalathantri *et al.* [31].

2.7.3 UHPC shear pocket

The compressive and tensile behaviors of UHPC significantly differ from those of NSC. The strength and ductility of the material are influenced by various factors, including the type and content of fibers [32]. Several analytical models have been suggested for expressing the stress–strain behaviors of UHPC [33]–[36]. The models utilized by Li *et al.*, [37] successfully captured the load-slip curves of studs in UHPC. Due to the similar UHPC mixture proportion and compressive strength, as well as the same type of fiber, the identical models were adopted in the present study to simulate the stress-strain response (Figure 9). The equations for compressive and tensile stresses of UHPC are given as follows in Equations (14) to (15).

$$\sigma_{c,U} = \begin{cases} f'_{c,U}\left[\frac{n\xi-\xi^2}{1+(n-2)\xi}\right] & (\xi \le \xi_0) \\ f'_{c,U}\left[\frac{\xi}{2(\xi-1)^2+\xi}\right] & (\xi > \xi_0) \end{cases} \tag{14}$$

Where $f'_{c,U}$ is the UHPC compressive strength. ξ is defined as $\varepsilon_{c,U}/\varepsilon_{0,U}$. Strain of UHPC at the peak stress $\varepsilon_{0,U}$ is set at 0.0035. $n = E_{0,U}/E_{sec}$, where $E_{0,U}$ is the initial elastic modulus of UHPC and E_{sec} is the secant modulus corresponding to the maximum stress.

$$\sigma_{t,U} = \begin{cases} \varepsilon_{t,U}\, E_{0,U} & (\varepsilon_{t,U} \le \varepsilon_{ct}) \\ f_{t,U} & (\varepsilon_{ct} < \varepsilon_{t,U} < \varepsilon_{pt}) \\ \frac{f_{t,U}}{(1+w/w_p)^p} & (w > 0) \end{cases} \tag{15}$$

Where $f_{t,U}$ is the UHPC tensile strength. ε_{ct} is the limit elastic strain and ε_{pt} is the tensile strain at the ultimate tensile strength. w is the crack opening. w_p and p are taken as 1 and 1.08, respectively [37].

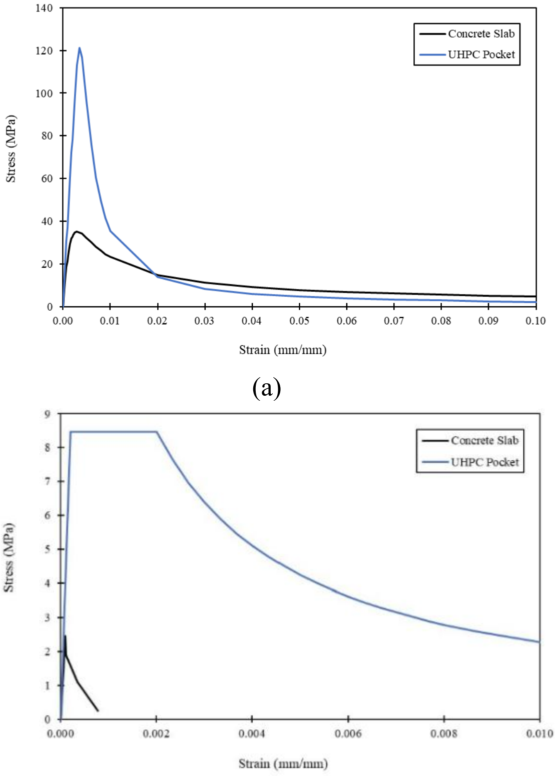

(a)

(b)

Figure 9: Concrete and UHPC property: (a) Compression Mode, (b) Tension Mode.

2.8 *Concrete damage plasticity model*

The concrete damage plasticity model in ABAQUS standard was performed on the concrete property, which was a concrete slab and a UHPC pocket. The parameter of the yield function and plastic flow was summarized in Table 4 [21], [30], [38], [39]. A study on the dilation angle of UHPC investigated values ranging from 30° to 55°. It was found that a dilation angle of 55° provided the best agreement with the experimental results of a UHPC beam test [40]. The dilation angles for normal-strength concrete (NSC) were investigated in the range of 30° to 40°. The results indicate that a dilation angle of 40° can simulate the experimental behavior with reasonable accuracy [41]. The dilation angle of 40° represented the highest and most reliable angle that could be calculated efficiently without introducing numerical errors. The stress–strain curve is presented in Figure 9. The parameters of the FE simulation can be identified as follows.

2.8.1 General

Concrete demonstrates nonlinear behavior, which includes plasticity and damage. These behaviors lead to a reduction in both stiffness and strength. The isotropic damage model in ABAQUS was used to represent stiffness degradation as expressed in Equation (16) [42].

$$\sigma = (1 - d)E_0(\varepsilon - \varepsilon^{pl}) \tag{16}$$

Where σ is the stress, ε is the total strain, ε^{pl} is the plastic strain, E_0 is the initial elastic stiffness (undamaged), d is the damage factor, f_c' is the concrete strength.

2.8.2 Yield function

The evaluation of the stress of state under tension and compression in plasticity is performed using the yield function defined in Equation (17). The yield function represents the effect of the stress of state in both tension and compression modes as illustrated in Figure 10(a). The yield function is further detailed in Equations (17) to (20) [40], [43].

$$F = \frac{1}{1-\alpha}\left(\bar{q} - 3\alpha\bar{p} + \beta(\tilde{\varepsilon}^{pl})\langle\hat{\bar{\sigma}}_{max}\rangle - \gamma\langle-\hat{\bar{\sigma}}_{max}\rangle\right) - \bar{\sigma}_c\left(\tilde{\varepsilon}_c^{pl}\right) = 0 \tag{17}$$

Where,

$$\alpha = \frac{(\sigma_{b0}/\sigma_{c0}) - 1}{2(\sigma_{b0}/\sigma_{c0}) - 1}; 0 \leq \alpha \leq 0.5 \tag{18}$$

$$\beta = \frac{\bar{\sigma}_c\left(\tilde{\varepsilon}_c^{pl}\right)}{\bar{\sigma}_t\left(\tilde{\varepsilon}_t^{pl}\right)}(1-\alpha) - (1+\alpha) \tag{19}$$

$$\gamma = \frac{3(1-K_c)}{2K_c - 1} \tag{20}$$

$\hat{\bar{\sigma}}_{max}$ is the maximum principal effective stress, σ_{b0}/σ_{c0} is the ratio of initial equiaxial compressive yield stress to initial uniaxial compressive yield stress (the default value is 1.16), K_c is the ratio of the second stress invariant on the tensile meridian, $\tilde{\varepsilon}_c^{pl}$ is the effective tensile cohesion stress, $\tilde{\varepsilon}_c^{pl}$ is the effective compressive cohesion stress.

2.8.3 Plastic flow

The plastic flow of the concrete damaged plasticity model in ABAQUS is defined by a non–associated flow rule where the flow potential function (*G*) differs from the yield function (*F*). The general flow potential function used in the model accounts for the effect of hydrostatic pressure, which is represented by the Drucker–Prager hyperbolic function, as defined in Equation **Error! Reference source not found.** [40], [43] and illustrated in Figure 10(b). The concrete damage plasticity (CDP) model in Abaqus recommends a dilation angle between 30° and 40° [44]

$$G = \sqrt{(\epsilon\sigma_{t0}tan\psi)^2 + \bar{q}^2} - \bar{p}tan\psi \tag{21}$$

Where ψ is the dilation angle in the *p–q* plane, σ_{t0} is the uniaxial tensile stress at failure, ϵ is a parameter, referred to as the eccentricity. The default flow potential eccentricity is $\epsilon = 0.1$ [31].

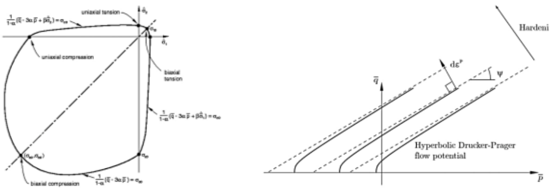

(a) (b)

Figure 10: Concrete plastic damage model: (a) yield surface, (b) general plastic flow of the Drucker–Prager hyperbolic function.

2.8.4 Damage plasticity

The damage plasticity describes the relationship between the plastic strain without stiffness degradation (ε^P) and the damage factor under tension

(d_t) and compression mode (d_c). The damage factor is governed by a user-defined constitutive law of concrete material in Equations (22) and (23) [42] and can be represented in Figure 11.

$$d_t = \frac{(1-k)\varepsilon^P}{(1-k)\varepsilon^P + \sigma/E_0};\ \dot{\varepsilon}^P \geq 0 \qquad (22)$$

$$d_c = \frac{\varepsilon^P - (\varepsilon - \tilde{\varepsilon}^e_{cr})}{\varepsilon^P - (\varepsilon - \tilde{\varepsilon}^e_{cr}) + \sigma/E_0};\ \dot{\varepsilon}^P \leq 0 \qquad (23)$$

Where k is proportional to the ratio of cohesion to the maximum cohesion of the material. In the case of uniaxial loading, this ratio can be expressed in Equation (24) [42].

$$k = \frac{\tilde{\varepsilon}^p}{\varepsilon^P} = \frac{c}{c_{max}} = \frac{\sigma}{f}\ ;\ \dot{\varepsilon}^P \geq 0 \qquad (24)$$

$\tilde{\varepsilon}^p$ is the plastic strain with stiffness degradation, ε^P is the plastic strain without stiffness degradation, d_t and d_c are the damage factors of tension and compression.

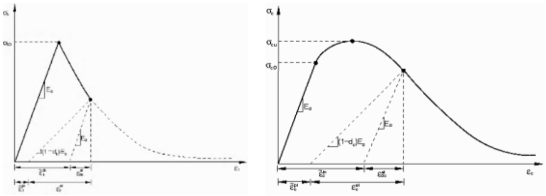
(a) (b)

Figure 11: stress–strain curve: (a) Concrete tension, (b) Concrete compression.

Table 4: Concrete property of concrete slab and UHPC Pocket.

Parameter	Value	
	Concrete Slab	UHPC Pocket
Young's modulus (GPa)	27.85	41.34
Poisson's ratio	0.18	0.216
Dilation Angle (deg)	40	40
Eccentricity	0.1	0.1
Fb0/fc0	1.16	1.16
K	0.667	0.677
Viscosity	0.0001	0.0001

2.9 *Interaction and boundary conditions*

The bonding interface between the concrete and metal materials was modeled using surface–to–surface contact with a friction coefficient of 0.4 [37]. This contact was specifically applied between the shear pocket surfaces and stud surfaces, between the angle confinement surfaces and the concrete slab surfaces, and between the concrete slab surface and the indenter surface. The friction coefficient of the bonding interface between the UHPC and concrete materials was 0.9 according to Eurocode 2 [45], which was specifically applied between the concrete slab surface and shear pocket surfaces. The surface–to–surface contact configuration of the model is shown in Figure 12. The reinforcement and hook bars were assigned as embedded regions within the concrete slab and shear pocket. A rigid body constraint was applied between the reference point and the surface of the stud plate hole to represent the pin connection (Figure 13).

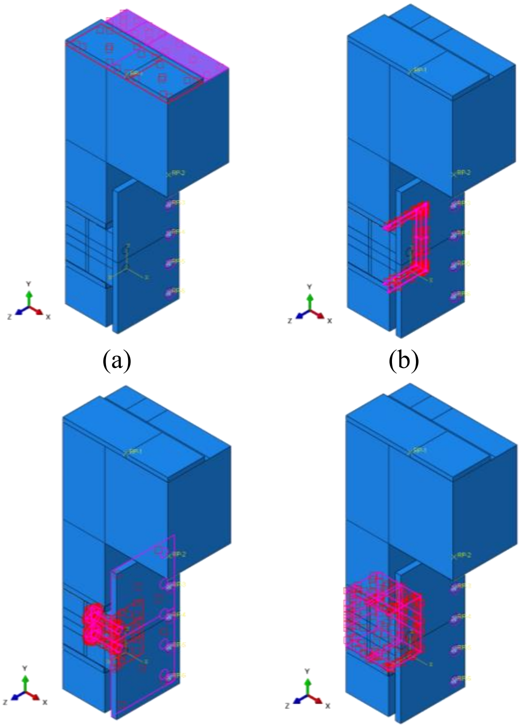
(a) (b)

(c) (d)

Figure 12: Surface–to–surface contact between: (a) the loading steel plate and concrete slab (b) the angle confinement and concrete slab, (c) the shear pocket and studs, (d) the shear pocket and concrete slab.

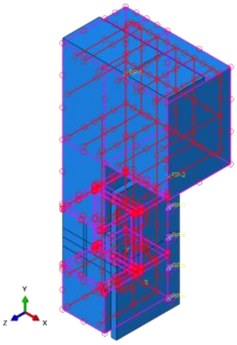

Figure 13: Reinforcement embedded region constraint to the concrete slab and shear pocket.

The mechanical stiffness of the push–off test was considered in the model, which has a vertical stiffness of 174.53 kN/mm [19]. The boundary conditions of the half model were defined using symmetry along the ZSYMM plane (U1 = UR1 = UR2 = 0) and the reference point at the stud plate hole was constrained with XSYMM symmetry (U1 = UR2 = UR3 = 0). The top surface of the indenter was coupled to a reference point where a vertical displacement was applied. The boundary conditions are illustrated in Figure 14.

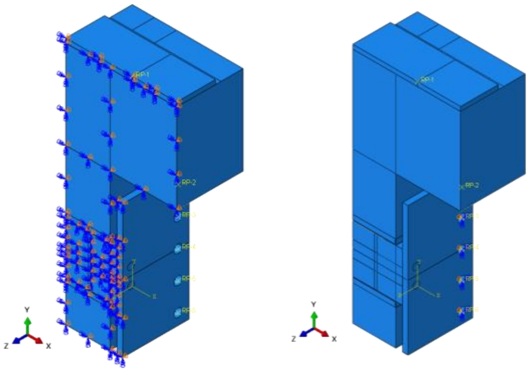
(a) (b)

Figure 14: Boundary conditions: (a) half model symmetry, (b) loading reference point at the stud plate hole symmetry.

3 Results and Discussion

3.1 *Material validation: Concrete damage plastic of concrete slab and UHPC*

The concrete compressive strength test of a cylinder for normal concrete material and a cubic for UHPC material was conducted to validate the material models in Section 2.7.2, 2.7.3 and 2.8. A comparison of ultimate strength between the concrete compressive strength test [19] and finite element (FE) simulations is presented in Table 5. The difference in ultimate compressive strength was lower than 2%. The compressive damage was graphically limited to 30% of the ultimate compressive strength [31], which corresponds to a compression damage factor of normal concrete material ($d_c = 0.7$) and UHPC material ($d_c = 0.671$). Figure 16 (a) observed cone-shaped cracking failure for normal concrete material, whereas UHPC material exhibited shattering and vertical cracking in Figure 16 (b). The simulation results showed good agreement with the experimental observations (Figure **15**).

Table 5: Compressive ultimate strength.

Material	Ultimate Strength (MPa)		Diff.
	Compressive Test [19]	FE Simulation	
Concrete	35.1	35.7	1.74%
UHPC	121.1	121.8	0.61%

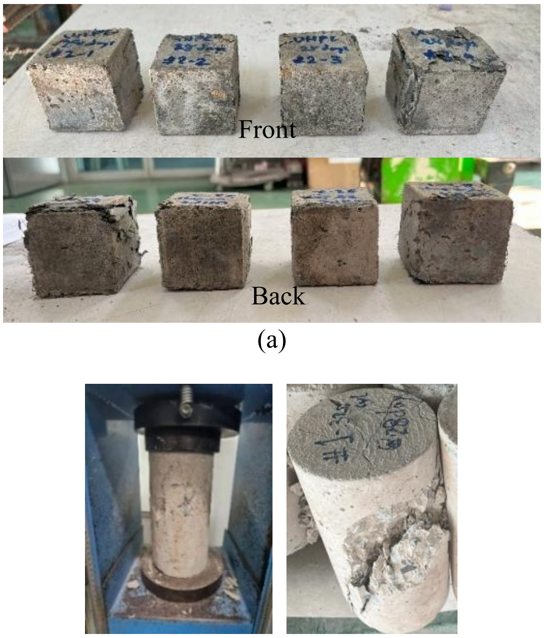

(a)

(b)

Figure 15: Failure mode of compressive strength test at 28 days [19]: (a) UHPC material (b) Normal concrete.

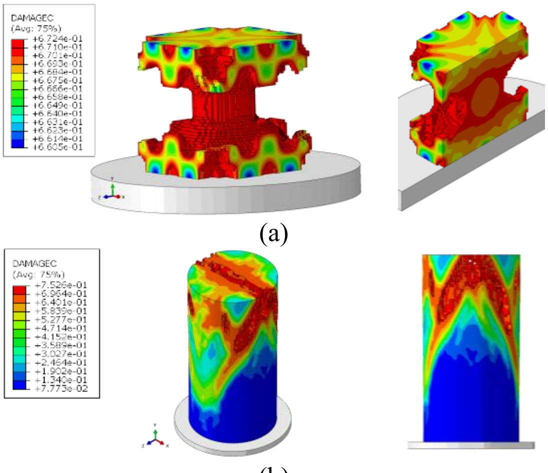

(a)

(b)

Figure 16: Failure mode of finite element (FE) simulations: (a) UHPC material (b) normal concrete.

3.2 *Model validation and parametric sensitivity for push–off test*

3.2.1 Element sizes analysis

The element size analysis was performed on specimen P-4-9x12-U with an eccentricity of 8" under the same test conditions. This model employed variable mesh sizes in the region where the concrete slab was in contact with the UHPC pockets, as described in section 2.6. Three (3) modes were compared for the ultimate load as follows: Mode 1 concrete slab element size 30 mm, Mode 2 concrete slab element size 20 to 30 mm, Mode 3 concrete slab element size 10 to 30 mm. Finite element (FE) simulations were developed based on the procedures described in Section 2.4. The analysis results of each ultimate load are summarized in Table 6. Mode 1 provided results most closely matching the experimental test values. The initial crack at 12 kgf [19] and the subsequent failure cracks are illustrated in Figure **17** and Figure **18**, respectively. A comparison with the experimental results in Figure 19 (a) shows that the crack pattern of Mode 3 closely resembles that observed in the test. Moreover, Figure 19 (b) and (c) present crack patterns for the test samples P-6-12-U and P-8-12x15-U, respectively. These premature failures are then validated with the simulation provided in the following section.

In summary, Mode 1 accurately predicted the ultimate load, whereas Mode 3 better captured damage propagation due to local damage, which also resulted in a lower predicted ultimate load. One possible reason is that with very fine meshes, the model becomes overly sensitive to small stress variations in the stiffness matrix at regions where tension damage occurs at the front and compression damage develops at the back. This sensitivity can lead to early localization of damage or premature element failure, resulting in an underestimated failure load in the simulation [7], [8], [46]. Therefore, an element size of 30 mm was selected for further simulations.

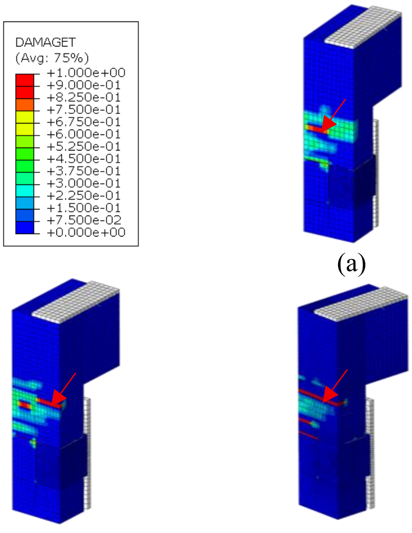

(a)

(b)

(c)

Figure 17: Tension damage at initial crack: (a) mode 1, (b) mode 2, (c) mode 3.

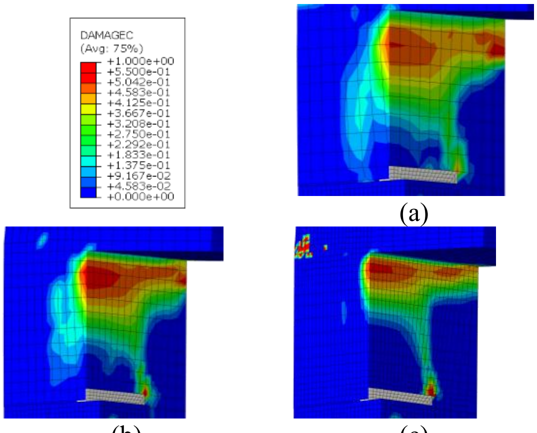

(a)

(b)

(c)

Figure 18: Compressive damage at failure crack: (a) mode 1, (b) mode 2, (c) mode 3.

Table 6: Ultimate loads with element size analysis.

Mode	Element size (mm)	Ultimate Loads (kgf)		Diff.
		Push-off Test [19]	FE Simulation	
1	30		54.0	1.8%
2	20 to 30	53	51.8	2.2%
3	10 to 30		48.6	8.3%

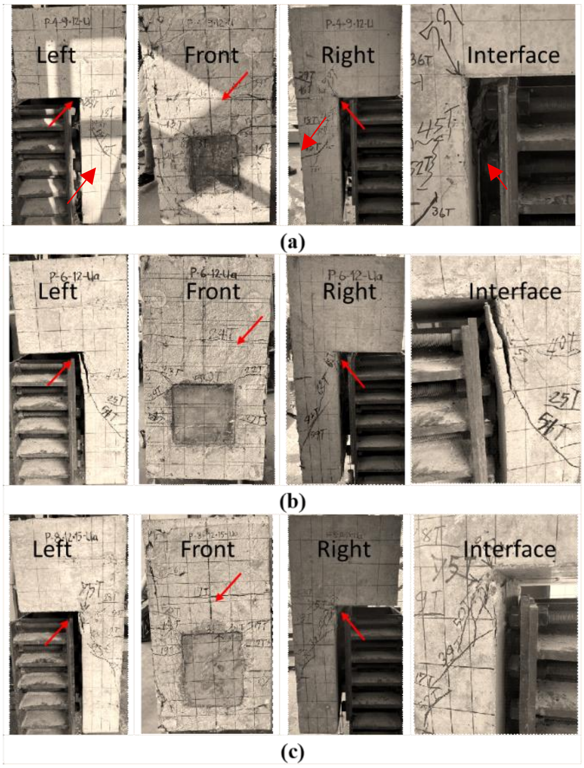

(a)

(b)

(c)

Figure 19: Crack patterns of specimen [19] (a) P-4-9×12-U (b) P-6-12-U (c) P-8-12×15-U.

3.2.2 *LVDT measurement location*

The location of the LVDT measurement influenced the slippage and stiffness response of the push-off simulation in the P-4-9x12-U with an eccentricity of 8" under the same test conditions [19]. Three (3) measuring points 4", 6", and 8" away from the front edge were studied as described in Section 2.5. The results can be summarized in terms of load-slip comparison as shown in Figure 20. Prior to the initial crack, the stiffness was found to be linear and consistent across all conditions. After the initial crack, the stiffness recorded at the LVDT located at the 8" eccentricity was noticeably lower than that at the 6" position, whereas the 4" position demonstrated the highest stiffness response. This was due to the eccentricity of the loading, which induced compressive forces and bending moments on the specimen. The bending moment led to specimen deflection, producing greater displacement readings at the LVDT located farther from the front edge [47]. However, the LVDT positioned at 6" corresponded well to the load-slip behavior of the experiment and therefore will be used for this study.

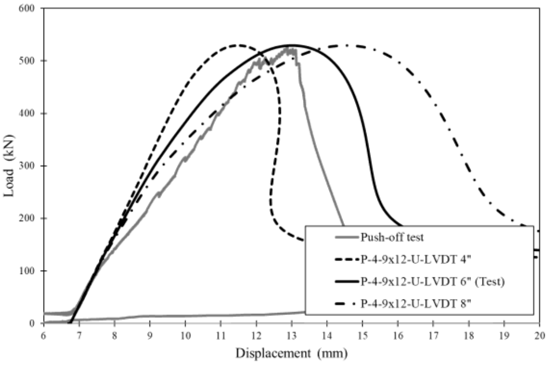

Figure 20: Load–Slip with different LVDT locations.

3.2.3 *Load location*

The push-off analysis was performed on specimens P-4-9×12-U, P-6-12-U, and P-8-12×15-U, with load applications at the center and at eccentricities of 6", 8", and 9", as described in section 2.5. The comparison of load–slip results between the push-off test at eccentricities of 8" [19] and the finite element (FE) simulation revealed consistent trends in the initial stiffness region, with a slight discrepancy observed after the onset of initial cracking. However, the ultimate load values obtained from both the experiments and simulations were in close agreement, except for the P-6-12-U model, which showed closer correspondence under the 9–inch off–center loading condition as illustrated in Figure 21.

The behavior of the push–off simulation can be explained as follows. The initial linear response is due to the initial stiffness of both the specimen structure and the testing equipment. As the loading progresses, the behavior becomes nonlinear due to the initiation of tensile damage in the concrete slab, as shown in Figure 22(a) for P-4-9×12-U, Figure 23(a) for P-6-12-U, and Figure 24(a) for P-8-12×15-U. The maximum strength is reached when compressive damage causes concrete crushing in the concrete slab, as illustrated in Figure

22(b) for P-4-9×12-U, Figure 23(b) for P-6-12-U, and Figure 24(b) for P-8-12×15-U. In the UHPC pocket, damage occurs in the form of tensile cracking [48], [49] around the stud area and debonding at the interface between the concrete slab and the UHPC pocket except model P-8-12×15-U, the failure mode is limited to interface debonding only as shown in Figure 22(c) for P-4-9×12-U, Figure 23(c) for P-6-12-U, and Figure 24(c) for P-8-12×15-U. The simulation exhibits the same type of damage as observed in the experimental test [19], as shown in Figure 19.

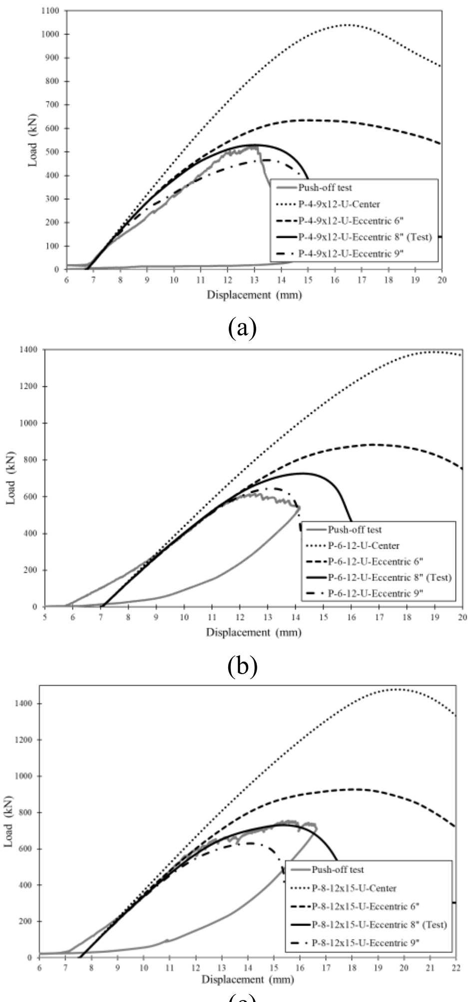

(a)

(b)

(c)

Figure 21: Load location of load-slip result: (a) P-4-9×12-U, (b) P-6-12-U, (c) P-8-12×15-U.

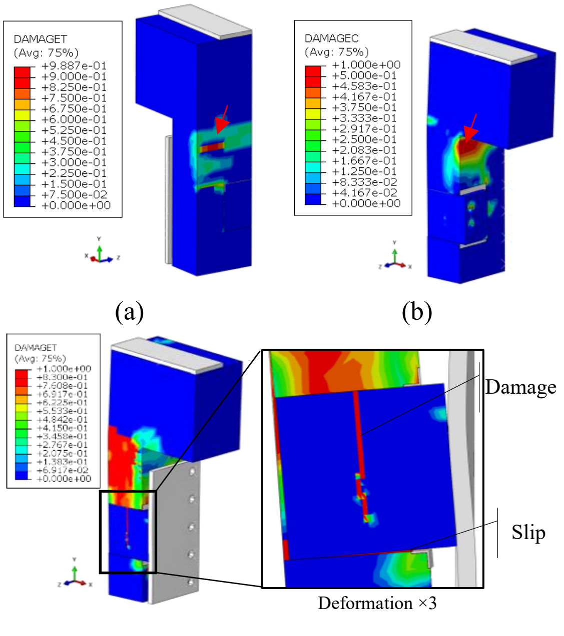

(a) (b)

(c)

Figure 22: Simulation model of P-4-9×12-U: (a) tension damage of concrete slab, (b) compressive damage of concrete slab, (c) tension damage of UHPC pocket.

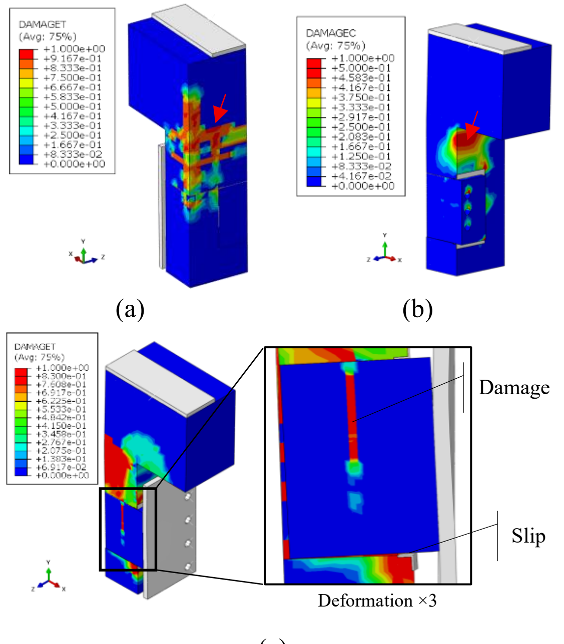

(a) (b)

(c)

Figure 23: Simulation model of P-6-12-U: (a) tension damage of concrete slab, (b) compressive damage of concrete slab, (c) tension damage of UHPC pocket.

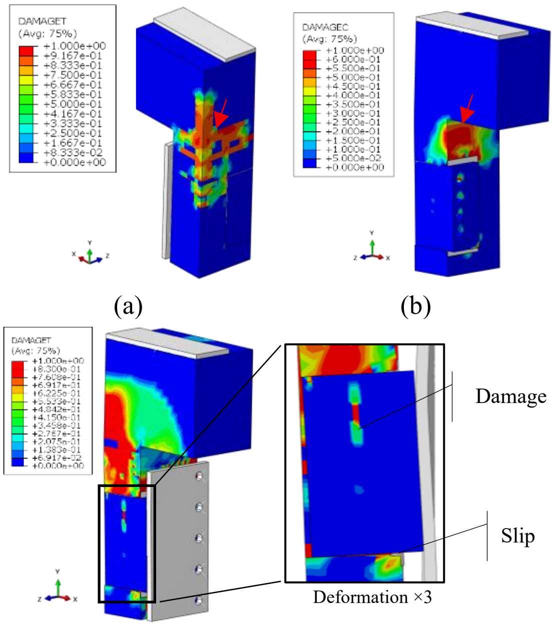

(a) (b)

(c)

Figure 24: Simulation model of P-8-12×15-U: (a) tension damage of concrete slab, (b) compressive damage of concrete slab, (c) tension damage of UHPC pocket.

Table 7: Ultimate loads drop

Model	Eccentric (in)	Ultimate Loads (kgf)	Ultimate Load Drop
P-4-9×12-U	Center	105.9	
	6	64.7	39%
	8[1]	54.0	49%
	9	47.4	55%
P-6-12-U	Center	142	
	6	91	36%
	8[1]	75	48%
	9	66	54%
P-8-12×15-U	Center	150.7	
	6	94.5	37%
	8[1]	74.5	51%
	9	64.2	57%

Note 1: The push–off test was conducted with the load applied at an eccentricity of 8" from the specimen's centerline [19].

The effect of eccentric loading directly resulted in a reduction of the ultimate load, as summarized in Table 7. This effect was sensitive to the distance of off-center loading [50]. At an eccentricity of 9", the ultimate load decreased by 36% to 57%, demonstrating a significant reduction in load-carrying capacity. As the eccentricity increased, the axial force (F_A) tended to rise, while the shear force (F_V) correspondingly declined, resulting in a lower load-carrying capacity under eccentric loading compared to direct shear loading. Therefore, it is recommended that the shear pocket design be configured to loads applied at the center. Whereas in cases with eccentric loading, the centric ultimate load can be determined by dividing the modification factors by percentages of ultimate load drop.

3.3 *Shear strength evaluation*

The shear strength was conducted on the models P-4-9×12-U, P-6-12-U, and P-8-12×15-U. The ultimate loads obtained from the push-off test [19] and the FE simulations showed good agreement, with differences of less than 2%, except for the model of P-6-12-U, which showed closer correspondence under the 9" eccentric loading condition. The types of damage observed in the simulations were generally consistent with the experimental results, except for specimen P-6-12-U, which exhibited only concrete crushing in the slab region. This discrepancy was attributed to transverse misalignment during testing, which introduced additional eccentric loading on the specimen. In the simulation, applying a 9–inch lateral offset effectively reproduced this condition, resulting in a close correlation with the observed experimental behavior. A summary of the comparative results is provided in Table 8.

Table 8: Ultimate loads and type of damage.

Model	Eccentric (in)	Push-off test [19]		Simulation		difference (%)
		Ultimate load (kgf)	Damage type[1]	Ultimate load (kgf)	Damage type[1]	
P-4-9×12-U	8[2]	53	FDPCC UHPCSC	54.0	FDPCC UHPCSC	1.8
P-6-12-U	8[2]	65	FDPCC	75	FDPCC UHPCSC	13.9
	9			66	FDPCC UHPCSC	1.1
P-8-12×15-U	8[2]	75	FDPCC	74.5	FDPCC	0.6

Note 1: FDPCC is the full–depth precast concrete crushing.
UHPCSC is the ultra–high–performance concrete shear cut.
Note 2: The push–off test was conducted with the load applied at an eccentricity of 8" from the specimen's centerline [19].

3.4 *Shear strength and eccentric load effect*

The effects of shear strength and eccentric loading were investigated by evaluating the shear force (F_V) and axial force (F_A) at the ultimate load [51]–[53]. Both forces were extracted at the stud plate of the FE simulation. The ultimate load obtained from the push–off test (F_{test}) was a combination of the direct shear force at the center of the FDPC panel only and the couple shear force due to eccentric loading [19], and the results were compared with the shear force provisions (P_u) specified in AASHTO LRFD [22]. The FE simulation results of the push-off test models under different load locations are presented in Table 9. In all cases, the ultimate load of the indenter was equivalent to the shear force at the stud plate. Noting that increasing eccentricity resulted in higher axial forces (pull-out between studs and a shear pocket). When the load was applied at the center of the FDPC panel, only shear force was present, and the axial force was zero. This condition was used to compare the ratio of shear force between the push-off test [19] and the AASHTO LRFD provisions [22], where the simulation results were found to be lower than both references. This means that the design based on simulation provides was more conservative than that obtained from both the experimental result and the AASHTO LRFD design equation. Therefore, this design approach ensures a higher level of safety.

Table 9: Shear strength and eccentric load effect.

Model	**Eccentric (in)^1**	**Shear force of push-off test [19], F_{test} (kgf)**	**Shear force of AASHTO LRFD [22], P_u (kgf)**	**Simulation**			**F_{test}/F_V**	**P_u/F_V**
				Shear force, F_V (kgf)	**Axial force, F_A (kgf)**	**Total force, T_{total} (kgf)**		
P-4-9×12-U	C	133	137	106	0	106	1.26	1.29
	6			65	8	65		
	8			54	12	55		
	9			47	13	49		
P-6-12-U	C	163	205	142	0	142	1.15	1.44
	6			91	14	92		
	8			75	18	77		
	9			66	19	69		
P-8-12×15-U	C	188	274	151	0	151	1.25	1.82
	6			95	16	96		
	8			75	19	77		
	9			64	19	67		

Note 1: C is the center of the FDPC panel.

3.5 *Angle confinement effect*

The effects of L–angle confinement were considered on the models P-4-9×12-U, P-6-12-U, and P-8-12×15-U with a constant eccentricity of 8 inches [19]. The comparison of the ultimate loads between with and without L–angle confinement models was summarized in 10 and represented in Figure 25(a)–(c) for all three cases. This indicates that the L–angle ring confinement enhanced the load–slip performance by approximately 4.8% to 15.1%. The increase in ultimate load was significantly influenced by the shear pocket width (P_W) as illustrated in Figure 1. A shear pocket width 9″ of P-4-9x12-U increased the ultimate load by approximately 15% while a 12″ width of P-6-12-U and P-8-12x15-U resulted in an increase of about 5% regardless of the number of studs. Noted that L–angle confinement with consistent sizes of 25×25×3 mm and two 12–mm diameter hook bars on each side of pocket were applied to all specimens and these were believed to be important factors to effectively increase shear resistance for the narrow pocket than the wider ones. Therefore, compatible sizes of L–angle confinement to the pocket width should be considered for the FDPC system, and more research studies are required for design guidelines [54].

In terms of load-slip behavior, the model without angle confinement exhibited a similar trend to that of the model with angle confinement, although the ultimate load was lower (Figure 25). The angle confinement did not affect the overall load-slip behavior but contributed only to an increase in the ultimate load. However, the L–angle confinement could sustain ductility effectively by around 4.6% for a cluster of 6– and 8–stud specimens, while highly effective for 11.1% for the cluster of the 4–stud specimen as concluded in Table 10.

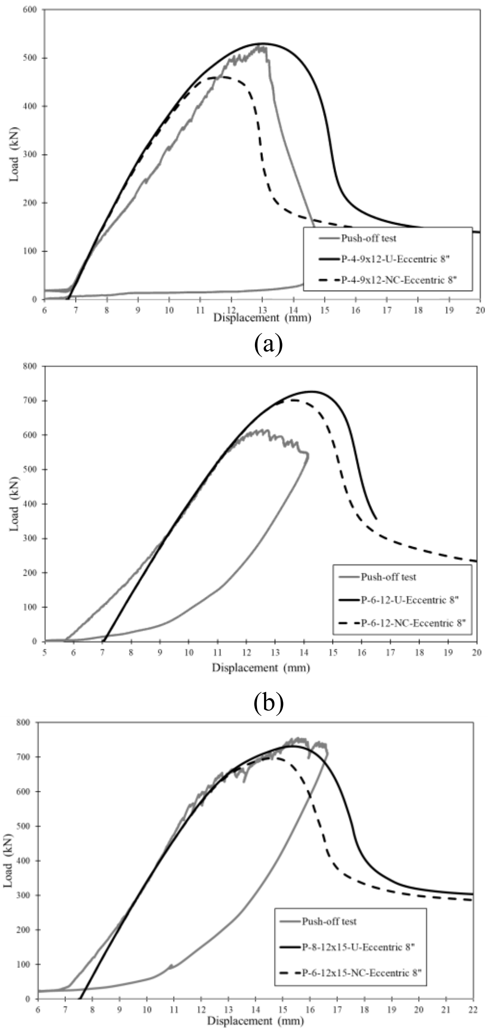

(a)

(b)

(c)

Figure 25: Angle confinement effect of load–slip result: (a) P-4-9×12-U, (b) P-6-12-U, (c) P-8-12×15-U.

Table 10: Ultimate loads and slips of angle confinement effect.

Model	**Ultimate load (kgf)**		**% Inc. (S)**	**Slip (mm)**		**% Inc. (D)**
	W/ L	**W/ O L**		**W/ L**	**W/ O L**	
P-4-9×12-U	54.0	46.9	15.1	13.0	11.7	11.1
P-6-12-U	75.0	71.5	4.9	14.3	13.6	5.1
P-8-12×15-U	74.5	71.1	4.8	15.3	14.7	4.1

Notes: W/ L = With L–angle confinement.
W/O L = Without L-angle confinement
% Inc. = Percent increase in terms of Strength (S) or Ductility (D).

4 Conclusions

This study developed and validated a finite element (FE) model to evaluate the structural behavior of Full–Depth Precast Concrete (FDPC) deck panels with Ultra–High–Performance Concrete (UHPC) shear pockets containing large–sized headed studs. However, high stress concentrations are often observed around UHPC-filled pockets, necessitating mitigation by confining with L–angle ring. Experiment results obtained from push–off tests under eccentric loading (P-4-9×12-U, P-6-12-U and P-8-12×15-U) were used to validate Finite Element (FE) simulations developed in ABAQUS/CAE. The validated FE models were then used to conduct parametric studies on shear strength, load–slip behavior, cracking development, and the effects of L–angle confinement. The FE model accurately predicted ultimate shear strength and damage, with the results being dependent on the selection of an appropriate mesh size. The model also successfully simulated key behaviors observed in the experiments, including the sensitivity of stiffness to LVDT placement and the significant reduction in load capacity as load eccentricity increased.

The parametric study further demonstrated that incorporating L–angle ring confinement enhanced both shear strength by up to 15% and ductility increased by 4–11%. However, when analyzed under centric loading, the model tended to underestimate shear strength compared to experimental results (15–20%) and the AASHTO LRFD equation (23–45%). Overall, the validated FE framework provides a reliable and efficient analytical tool for predicting the composite behavior of FDPC deck panels with UHPC shear pockets. While the results demonstrate strong agreement with experimental findings, further studies are recommended to establish practical design and construction guidelines, particularly under fatigue and cyclic loading conditions.

Acknowledgments

This research was funded by King Mongkut's University of Technology North Bangkok, Contract no. KMUTNB–68–BASIC–11. The authors would like to express gratitude to all staff involved in this research, including the Faculty of Technical Education, Faculty of Engineering, and Operations Center of Research and Development for Innovation, Invention and Modern Technology, KMUTNB Techno Park.

Author Contributions

K.T.I., K.C.S., S.R.P.: Conceptualization; K.T.I., K.C.S., N.R.C.: methodology; K.T.I., K.C.S.: research design; K.T.I., K.C.S., N.R.C., S.R.P.: data analysis, investigation, writing–original draft, writing–reviewing and editing; K.C.S.: funding acquisition, project administration. All authors have read and agreed to the published version of the manuscript.

Conflicts of Interest

The authors declare no conflict of interest, no known competing financial interests or personal relationships that could have appeared to influence the work reported in this paper.

Declaration of generative AI and AI–assisted technologies in the writing process

The authors utilized the ChatGPT tool to enhance the language and readability of the manuscript.

References

[1] T. Yamane, M. K. Tadros, S. S. Badie, and M. C. Baishya, "Full-depth precast prestressed concrete bridge deck system," *PCI Journal*, vol. 43, no. 3, pp. 50–66, 1998.

[2] K. E. Hanna, G. Morcous, and M. K. Tadros, "Rapid construction of Pacific Street Bridge," Nebraska Department of Roads, Lincoln, NE, USA, Rep. SPR-PL-1 (037) P587, 2010.

[3] K. E. Hanna, G. Morcous, and M. K. Tadros, "Standardized precast prestressed concrete panels for bridge decks," in *Concrete Bridge Conference*, 2008.

[4] B. A. Graybeal, "Ultra-high-performance concrete connections for precast concrete bridge decks," *PCI Journal*, vol. 59, no. 4, pp. 48–62, 2014, doi: 10.15554/pcij.09012014.48.62.

[5] B. A. Graybeal, "Ultra-high performance concrete composite connections for precast concrete bridge decks," Federal Highway Administration, Office of Infrastructure Research and Development, McLean, VA, Tech. Rep. FHWA-HRT-12-041, 2012.

[6] D. Garber and E. Shahrokhinasab, "Performance comparison of in-service, full-depth precast concrete deck panels to cast-in-place decks," Florida Int'l University, Miami, FL, Tech. Rep. ABC-UTC-2013-C3-FIU03-Final, Mar. 2019.

[7] L. Chen, J. Yan, Z. Wu, D. Yang, J. Li, and N. Xiang, "Experimental and numerical study on shear behavior of shear pockets between ultra-high-performance and normal concrete for precast girder bridges," *Structures*, vol. 55, pp. 1645–1658, 2023.

[8] A. Yuan et al., "Comparative shear performance of ultra-high-performance concrete filled pocket and longitudinal trough connector of precast composite girder with full-depth deck," *Structural Concrete*, vol. 25, no. 6, pp. 4795–4811, 2024.

[9] Z. Ren et al., "Shear behavior of precast bridge deck panels with UHPC wet joints," *Engineering Structures*, vol. 316, 2024, Art. no. 118569, doi: 10.1016/j.engstruct.2024.118569.

[10] R. Zhong et al., "Durability of micro-cracked UHPC subjected to coupled freeze-thaw and chloride salt attacks," *Cement and Concrete Composites*, vol. 135, Art. no. 104835, Feb. 2024, doi: 10.1016/j.cemconcomp.2024.105471.

[11] B. Graybeal, "Design and construction of field-cast UHPC connections," Federal Highway Administration, McLean, VA, Tech. Rep. FHWA-HRT-19-011, 2019.

[12] S. S. Badie et al., "Large shear studs for composite action in steel bridge girders," *Journal of Bridge Engineering*, vol. 7, no. 3, pp. 195–203, 2002, doi: 10.1061/(ASCE)1084-0702(2002)7:3(195).

[13] J. Qi, Y. Hu, J. Wang, and W. Li, "Behavior and strength of headed stud shear connectors in ultra-high performance concrete of composite bridges," *Frontiers of Structural and Civil Engineering*, vol. 13, no. 5, pp. 1138–1149, 2019, doi: 10.1007/s11709-019-0542-6.

[14] S. S. Badie, A. F. M. Girgis, M. K. Tadros, and K. Sriboonma, "Full-scale testing for composite slab/beam systems made with extended stud spacing," *Journal of Bridge Engineering*, vol. 16, no. 5, pp. 653–661, 2011.

[15] J. Wang, Q. Xu, Y. Yao, J. Qi, and H. Xiu, "Static behavior of grouped large headed stud-UHPC shear connectors in composite structures," *Composite Structures*, vol. 206, pp.

202–214, 2018, doi: 10.1016/j.compstruct.2018.08.014.

[16] K. Sriboonma and S. S. Badie, "Practical steel confinements for wildly spaced clustered large stud shear connectors in composite bridge deck panel systems," in *The Steel Conference (NASCC)*, Florida, USA, May 12–15, 2010.

[17] K. Sriboonma and S. Pornpeerakeat, "Experimental investigation of steel confinement of clustered large-size stud shear connector in full-depth precast bridge deck panel," *Key Engineering Materials*, vol. 856, pp. 99–105, Aug., 2020.

[18] K. Sriboonma, "Fatigue behavior of steel ring confinement for a clustered stud shear connector in full-depth precast concrete bridge deck panel," *Materials Today: Proceedings*, vol. 52, pp. 2555–2561, Jan., 2022.

[19] K. Sriboonma, N. Khomwan, K. Chaimoon, and K. Rodsin, "Shear behavior of ultra-high-performance concrete shear pockets with large-sized studs in full-depth precast concrete bridge deck under push-off tests," *Applied Science and Engineering Progress*, vol. 19, no. 3, 2026, Art. no. 8014.

[20] H. Jiang et al., "Shear performance of headless studs in ultra-high performance concrete bridge deck," *Frontiers in Materials*, vol. 11, Mar. 2024, doi: 10.3389/fmats.2024.1379386.

[21] K. Sriboonma, C. Boonmee, S. Pornpeerakeat, K. Rodsin, and N. Chaiwino, "Finite element investigation of angle ring confinement for clustered large-size stud shear connector in full-depth precast concrete bridge deck panel," *Applied Science and Engineering Progress*, vol. 17, no. 1, 2024, Art. no. 6914, doi: 10.14416/j.asep.2023.06.003.

[22] American Association of State Highway and Transportation Officials, *LRFD Bridge Design Specifications*, 6th ed., Washington, DC: AASHTO, 2012.

[23] S. Pornpeerakeat, K. Sriboonma, and A. Chaikittiratana, "A modified strain–displacement method for high accuracy 8-node solid finite element," *Applied Science and Engineering Progress*, vol. 15, no. 1, 2022, Art. no. 3784, doi: 10.14416/j.asep.2020.12.003.

[24] American Petroleum Institute, *API 579-1/ASME FFS-1: Fitness-for-Service*, 3rd ed., Washington, DC: American Petroleum Institute, 2016.

[25] P. Desayi and S. Krishnan, "Equation for the stress-strain curve of concrete," *ACI Journal Proceedings*, vol. 61, no. 3, pp. 345–350, Mar. 1964.

[26] D. J. Carreira and K. H. Chu, "Stress-strain relationship for plain concrete in compression," *ACI Journal Proceedings*, vol. 82, no. 6, pp. 797–804, Nov. 1985.

[27] D. A. Hordijk, "Local approach to fatigue of concrete," Ph.D. dissertation, Delft University of Technology, Delft, Netherlands, 1991.

[28] A. Belarbi and T. T. Hsu, "Constitutive laws of concrete in tension and reinforcing bars stiffened by concrete," *Structural Journal*, vol. 91, no. 4, pp. 465–474, Jul. 1994.

[29] R. Nayal and H. A. Rasheed, "Tension stiffening model for concrete beams reinforced with steel and FRP bars," *Journal of Materials in Civil Engineering*, vol. 18, no. 6, pp. 831–841, Dec. 2006.

[30] *Building Code Requirements for Structural Concrete and Commentary*, ACI 318-14, ACI Committee 318, 2014.

[31] B. Wahalathantri, D. Thambiratnam, T. Chan, and S. Fawzia, "A material model for flexural crack simulation in reinforced concrete elements using ABAQUS," in *Proceedings of the First International Conference on Engineering, Designing and Developing the Built Environment for Sustainable Wellbeing*, 2011, pp. 260–264.

[32] S. Pyo, S. El-Tawil, and A. E. Naaman, "Direct tensile behavior of ultra high performance fiber reinforced concrete (UHP-FRC) at high strain rates," *Cement and Concrete Research*, vol. 88, pp. 144–156, Oct. 2016.

[33] D. A. Fanella and A. E. Naaman, "Stress-strain properties of fiber reinforced mortar in compression," *ACI Journal Proceedings*, vol. 82, no. 4, pp. 475–483, Jul. 1985.

[34] M. A. Mansur, M. S. Chin, and T. H. Wee, "Stress-strain relationship of high-strength fiber concrete in compression," *Journal of Materials in Civil Engineering*, vol. 11, no. 1, pp. 21–29, Feb. 1999.

[35] B. A. Graybeal, "Compressive behavior of ultra-high-performance fiber-reinforced concrete," *ACI Materials Journal*, vol. 104, no. 2, pp. 146–152, Mar. 2007.

[36] Z. Shi, Q. Su, F. Kavoura, and M. Veljkovic, "Uniaxial tensile response and tensile

constitutive model of ultra-high performance concrete containing coarse aggregate (CA-UHPC)," *Cement and Concrete Composites*, vol. 136, Feb. 2023, Art. no. 104878, doi: 10.1016/j.cemconcomp.2022.104878.

[37] Y. Li, S. Wang, G. Zhao, Y. Ma, D. Guo, J. Luo, Z. Fang, and E. Fang, "Shear behavior of short studs in steel-thin ultrahigh-performance concrete composite structures," *Case Studies in Construction Materials*, vol. 19, Dec. 2023, Art. no. e02391.

[38] S. Nasrin and A. Ibrahim, "Finite-element modeling of UHPC hybrid bridge deck connections," *International Journal of Advanced Structural Engineering*, vol. 10, no. 3, pp. 199–210, 2018.

[39] S. Michał and W. Andrzej, "Calibration of the CDP model parameters in Abaqus," in *World Congress on Advances in Structural Engineering and Mechanics(ASEM)*, Incheon, Korea, 2015.

[40] M. Fakeh, A. Jawdhari, and A. Fam, "Recommended concrete damage plasticity parameters and constitutive models for UHPC in ABAQUS," *Engineering Structures*, vol. 333, 2025, Art. no. 120154.

[41] Y. Jia and J. C. Chiang, "Finite element analysis of punching shear of reinforced concrete slab–column connections with shear reinforcement," *Applied Sciences*, vol. 12, no. 19, 2022, Art. no. 9584.

[42] Y. Tao and J. F. Chen, "Concrete damage plasticity model for modeling FRP-to-concrete bond behavior," *Journal of Composites for Construction Construction*, vol. 19, no. 1, Art. no. 04014026, 2015.

[43] *ABAQUS 2016: Theory Manual*, Dassault Systems, Providence, RI, USA, 2016.

[44] C. Le Thanh, H. L. Minh, and T. Sang-To, "A nonlinear concrete damaged plasticity model for simulation of reinforced concrete structures using ABAQUS," *Fracture and Structural Integrity*, vol. 16, no. 59, pp. 232–242, 2022.

[45] M. Abo El-Khier and G. Morcous, "Friction and cohesion interface shear factors of ultra-high-performance concrete (UHPC) cast on hardened conventional concrete," *Buildings*, vol. 13, no. 5, 2023, Art. no. 1253.

[46] J. Guo, Z. Zhou, Y. Zou, Z. Zhang, and J. Jiang, "Finite element analysis of precast concrete deck-steel beam-connection concrete (PCSC) connectors using ultra-high performance concrete (UHPC) for the composite beam," *Buildings*, vol. 12, no. 9, 2022, Art. no. 1402.

[47] J. Bian, J. Zhang, L. Zhao, W. Gan, and W. Cao, "Shear performance of reinforced shear pocket joint in light steel—recycled concrete composite floor," *Buildings*, vol. 15, no. 13, Art. no. 2267, 2025.

[48] G. Gullì, R. Bertino, F. Grungo, D. Palamara, P. Bruzzaniti, and L. Calabrese, "Flexural toughening of hooked-end steel fibers reinforced mortars," *Applied Science and Engineering Progress*, vol. 17, no. 2, pp. 123–135, 2024, doi: 10.14416/j.asep.2023.11.004.

[49] A. Dhandapani, S. Krishnasamy, R. Nagarajan, S. M. K. Thiagamani, and C. Muthukumar, "Study on the inter-laminar shear strength and contact angle of glass fiber/ABS and glass fiber/carbon fiber/ABS hybrid composites," *Applied Science and Engineering Progress*, vol. 16, no. 3, pp. 145–153, 2023, doi: 10.14416/j.asep.2023.02.004.

[50] D. Vargas, E. O. Lantsoght, and A. S. Genikomsou, "Flat slabs in eccentric punching shear: Experimental database and code analysis," *Buildings*, vol. 12, no. 12, 2022, Art. no. 2092.

[51] G. Wang, B. Xian, F. Ma, and S. Fang, "Shear performance of prefabricated steel ultra-high-performance concrete (UHPC) composite beams under combined tensile and shear loads: single embedded nut bolts vs. studs," *Buildings*, vol. 14, no. 8, 2024, Art. no. 2425.

[52] H. Wang, N. Wang, X. G. Liu, Q. R. Yue, J. L. Yan, and Y. Zhang, "Effects of UHPC shear key on strengthening shear performances of wet joint in prefabricated composite beams," *Engineering Structures*, vol. 299, 2024, Art. no. 117130.

[53] Z. Lin, Y. Liu, and J. He, "Behavior of stud connectors under combined shear and tension loads," *Engineering Structures*, vol. 81, pp. 362–376, 2014

[54] G. Morcous and R. Tawadrous, "Precast concrete deck-to-girder mechanical connection for accelerated bridge construction," *PCI Journal*, vol. 65, no. 6, pp. 47–64, 2020.